Time Scales of Porphyry Cu Deposit Formation: Insights from Titanium Diffusion in Quartz

Celestine N. Mercer,[1],[†],[*] Mark H. Reed,[1] and Cameron M. Mercer[2]

[1] *Department of Geological Sciences, 1272 University of Oregon, Eugene, Oregon 97403*

[2] *School of Earth & Space Exploration, Arizona State University, Tempe, Arizona 85287*

Abstract

Porphyry dikes and hydrothermal veins from the porphyry Cu-Mo deposit at Butte, Montana, contain multiple generations of quartz that are distinct in scanning electron microscope-cathodoluminescence (SEM-CL) images and in Ti concentrations. A comparison of microprobe trace element profiles and maps to SEM-CL images shows that the concentration of Ti in quartz correlates positively with CL brightness but Al, K, and Fe do not. After calibrating CL brightness in relation to Ti concentration, we use the brightness gradient between different quartz generations as a proxy for Ti gradients that we model to determine time scales of quartz formation and cooling. Model results indicate that time scales of porphyry magma residence are ~1,000s of years and time scales from porphyry quartz phenocryst rim formation to porphyry dike injection and cooling are ~10s of years. Time scales for the formation and cooling of various generations of hydrothermal vein quartz range from 10s to 10,000s of years. These time scales are considerably shorter than the ~0.6 m.y. overall time frame for each porphyry-style mineralization pulse determined from isotopic studies at Butte, Montana. Simple heat conduction models provide a temporal reference point to compare chemical diffusion time scales, and we find that they support short dike and vein formation time scales. We interpret these relatively short time scales to indicate that the Butte porphyry deposit formed by short-lived episodes of hydrofracturing, dike injection, and vein formation, each with discrete thermal pulses, which repeated over the ~3 m.y. generation of the deposit.

Introduction

Porphyry Cu deposits around the world show clear evidence that they form where fluid overpressurization in a magmatic cupola produces pulses of hydrofracturing, porphyry dike injection, brecciation, and stockwork veining (Burnham, 1979; Titley and Beane, 1981; Dilles, 1987; Cline and Bodnar, 1991; Seedorff et al., 2005; Sinclair, 2007; Sillitoe, 2010). Metal- and sulfur-rich aqueous fluids permeate the fractured rock, causing host-rock alteration and depositing quartz and Cu and Mo sulfides in stockwork veins and breccias. Decades of study of porphyry deposits have advanced our knowledge of magmatic and tectonic controls on porphyry mineralization (e.g., Cloos, 2001; Tosdal and Richards, 2001; Guillou-Frottier and Burov, 2003; Richards, 2003; Candela and Piccoli, 2005; Cooke et al., 2005), hydrothermal alteration zones, mineralization patterns, and hydrothermal fluid evolution (e.g., Dilles and Einaudi, 1992; Redmond et al., 2004; Landtwing et al., 2005; Seedorff et al., 2005; Rusk et al., 2008b; Reed and Palandri, 2010; Reed et al., 2013), yet much remains to be understood about the time scales of porphyry Cu processes.

In this study, we examine the fundamental question of timing and duration of porphyry dike magmatism and hydrothermal vein formation from the porphyry Cu-Mo deposit at Butte, Montana (Fig. 1).

Several studies have provided absolute age constraints for the porphyry dike injections and mineralization at Butte. The deposit is hosted by the 77 to 75 Ma Butte Granite (Lund et al., 2002; Dilles et al., 2003). U-Pb zircon ages suggest that the Steward porphyry dike, which is contemporaneous with porphyry-style "pre-Main stage" mineralization (Brimhall, 1973), dates to 65.7 (±0.9) Ma (Lund et al., 2002). Pre-Main stage mineralization occurred over a span of ~3 m.y. in two successive pulses, each lasting a maximum of ~0.6 m.y. The first pulse produced the Pittsmont dome from 66.4 to 65.8 (±0.2) Ma while the second pulse produced the Anaconda dome from 64.5 to 63.9 Ma (Fig. 2; Snee et al., 1999; Dilles, writ. commun., 2008). Crosscutting relationships, U-Pb monazite ages, and Ar-Ar ages show that pre-Main stage porphyry mineralization was followed by the Modoc porphyry plug injection at 64 (±1) Ma (Meyer et al., 1968; Dilles et al., 2003), after which "Main stage" base metal lodes formed from 63.0 to 61.5 (±0.2) Ma (Snee et al., 1999; Dilles, writ. commun., 2008). U-Pb zircon dates show that all of these magmatic and hydrothermal generations were cut by postmineralization

[†] Corresponding author: e-mail, cmercer@usgs.gov

[*] Current address: U.S. Geological Survey, Box 25046, Denver Federal Center, MS-973, Denver, Colorado 80225.
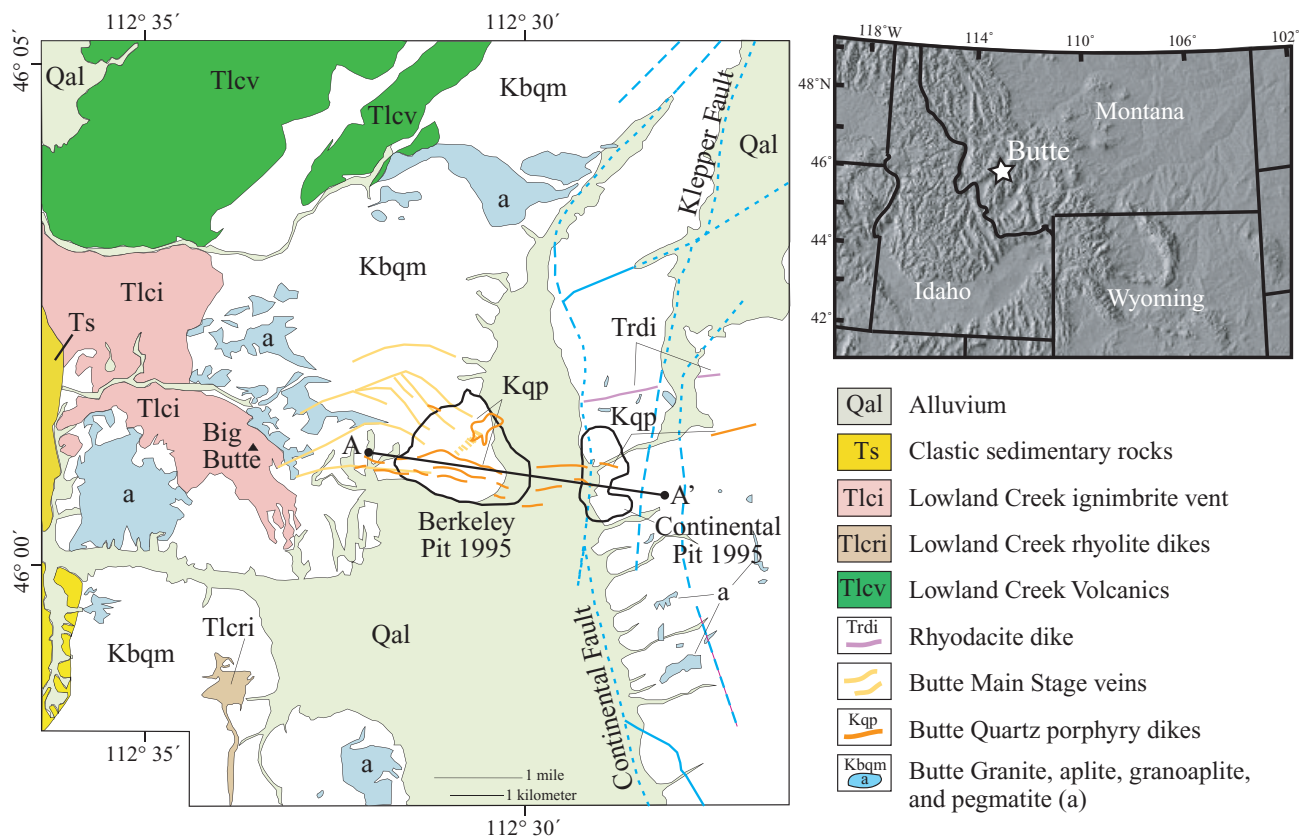
FIG. 1. Location map and regional geologic setting of the Butte district (modified from Rusk et al., 2008b). Line A-A' denotes cross section in Figure 2.
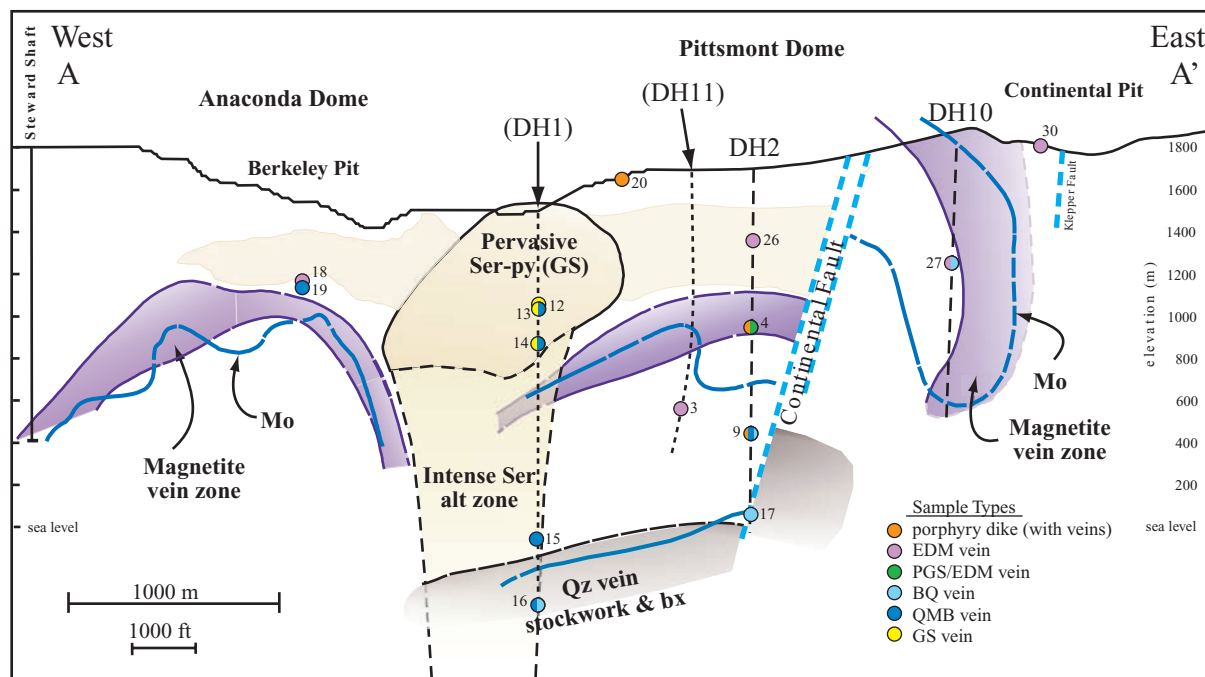

FIG. 2. West-east cross section (A-A') of pre-Main stage porphyry Cu-Mo mineralization at Butte. The Anaconda and Pitts-mont domes are defined by zones of abundant magnetite veins (shaded purple) and by Mo-grade contours (blue lines). The Continental fault displaces the Pittsmont dome upward by ~1,300 m. Dashed lines indicate drill holes (those in parentheses indicate holes projected into this cross section). Colored circles show locations of samples analyzed for this study. Circles with multiple colors represent samples that contain crosscutting veins representative of different vein types. Map numbers correspond to sample numbers and descriptions in Table 1 and Mercer and Reed (2013). Abbreviations are explained in Table 1.

rhyolite dikes between 62.7 (±1.5; Lund et al., 2005) and 60.4 (±0.3) Ma (Dilles et al., 2003).

These absolute age constraints reveal that the deeper portions of the pre-Main stage deposit cooled later than the shallower portions (Snee et al., 1999), but it is not yet clear how long individual dike injections and stockwork veins took to form during each ~0.6 m.y. time window. A widely accepted model for porphyry Cu formation is that fractured, pervasively heated host rock overlying the magma source reacts with a single pulse of high-temperature magmatic fluids for ~1 m.y., during which multiple generations of crosscutting hydrothermal veins form with progressive cooling of the fluid (e.g., Cathles and Shannon, 2007). Contrasting with this notion, modeling of diffusion and reaction in sericitic alteration envelopes (1–2 cm) from Butte, which are common in pre-Main stage pyrite-quartz stockwork veins, suggests that alteration envelopes could have formed in <100 years (Geiger et al., 2002). If this time span applies to alteration along other stockwork vein types as well, then a model of short lived, episodic fluid injections that span ~1 m.y. may be a more accurate explanation for porphyry Cu deposit generation (e.g., Mercer and Reed, 2013).

Diffusion modeling of chemical gradients in minerals has rarely been applied to hydrothermal systems (Costa et al., 2008), but it has been a successful chronological tool used to constrain time scales of igneous and metamorphic processes (e.g., Turner and Costa, 2007; Costa et al., 2008; Spear et al., 2012). For example, Ti-zoning within single quartz phenocrysts indicates magma residence and crystal mush reactivation time scales for silicic systems ranging from 1,000s to 10,000s of years (e.g., Whakamaru and Rangitaiki ignimbrites, Matthews et al., 2012; Bandelier Tuff, Wilcock et al., 2013), whereas time scales for mafic magma recharge leading to silicic volcanic eruptions may occur over much shorter time scales of months to decades (e.g., Bishop Tuff, Wark et al., 2007; Whakamaru and Rangitaiki ignimbrites, Matthews et al., 2012). In this study, we build on our thermobarometry results presented in Mercer and Reed (2013) and apply diffusion modeling of Ti gradients in quartz to investigate the formation and cooling time scales of quartz from porphyry dike intrusions and a variety of pre-Main stage hydrothermal veins from Butte.

Scanning electron microscope-cathodoluminescence (SEM-CL) images reveal detailed quartz growth histories, and microprobe trace element analyses verify that Ti is the primary CL activator in high-temperature magmatic and hydrothermal quartz from Butte. By calibrating relative CL brightness to corresponding Ti concentrations, we use brightness gradients as a proxy for Ti gradients within our samples. We model the diffusion of Ti between distinct quartz generations to determine the time scales of quartz precipitation and cooling for magmatic and hydrothermal quartz throughout the porphyry deposit. To create a temporal reference point to compare to chemical diffusion time scales, we model heat conduction thermal profiles for a rhyolitic dike, quartz vein, and hydrothermal fluid injection.

Geologic Setting and Sample Selection

The Butte porphyry Cu-Mo deposit is centered on an east-west–striking swarm of early Paleocene rhyolitic quartz porphyry dikes (Fig. 1) that intruded the Late Cretaceous Butte Granite (Meyer et al., 1968; Brimhall, 1973; Lund et al., 2002; Dilles et al., 2003; Lund et al., 2005; du Bray et al., 2012). Pre-Main stage Cu and Mo mineralization lies in two zoned domes, the Pittsmont and the Anaconda domes, which are each ~2 km in diameter (Reed et al., 2013). Both the Pittsmont and Anaconda domes have typical porphyry-style concentric, overlapping alteration zones composed of cm-scale stockwork veins (e.g., Meyer et al., 1968; Brimhall, 1973; Roberts, 1975). These domes are separated by a 1.2-km bulb-shaped zone of pyrite-quartz veins with intense gray sericitic alteration that extends downward more than 2 km (e.g., Rusk et al., 2008b; Reed et al., 2013).

We selected 15 samples from the Butte deposit, encompassing two porphyry dikes and a variety of stockwork vein types from both mineralized domes and the central zone of intense sericitic alteration (Table 1; Fig. 2). Most samples are drill core from depths of 350 to 2,070 m below the surface, and a few samples are from surface pit exposures (Fig. 2). Quartz porphyry dike samples are hydrothermally altered and cut by stockwork veins. Vein samples include barren quartz and quartz-molybdenite veins that lack alteration envelopes, quartz-chalcopyrite-pyrite veins with early dark micaceous (Meyer, 1965) alteration envelopes, and pyrite-quartz veins with gray sericitic alteration envelopes (Reed et al., 2013). These samples are a subset of those described by Mercer and Reed (2013) that contain good examples of quartz growth bands and crosscutting generations of vein quartz suitable for Ti diffusion modeling to provide constraints on the timing and duration of hydrofracturing, porphyry dike injections, and vein formation.

Methods

SEM-cathodoluminescence

We acquired SEM images at the University of Oregon using an FEI Quanta 200 FEG scanning electron microscope equipped with an Oxford Instruments CL detector. The CL detector has a spectral range of ~200 to ~800 nm; however, the spectral response drops off below ~250 and above ~500 nm and therefore it is most efficient in gathering light in ultraviolet and blue wavelengths rather than in red and infrared wavelengths. CL emissions from Ti in quartz are characteristically blue (Götze et al., 2001; Götte et al., 2011; Leeman et al., 2012; Rusk, 2012), so we recorded grayscale SEM-CL images captured using a blue band-pass filter (440–480 nm) to obtain the clearest SEM-CL images that incorporated Ti emissions and minimized microprobe beam damage spots, surface contamination, and bright streaks from highly fluorescent minerals (e.g., apatite) that otherwise oversaturated the signal. Doubly polished 200-μm-thick sections were carbon coated (15–20 nm) and analyzed at 10 keV with a beam current of 0.5 to 5 nA. We collected more than 300 SEM-CL images of igneous and hydrothermal quartz with corresponding SEM-backscattered electron and secondary electron images.

Microprobe trace element traverses and mapping

Trace element concentrations in quartz were measured at the University of Oregon using a Cameca SX-100 electron microprobe operated using one setup optimized for

TABLE 1. Sample Locations, Descriptions, and Modeled SEM-CL Boundary Types

Location	Map no.	Sample no.	Host rock	Vein//alteration type	Modeled SEM-CL boundary types					
					(1) Phenocryst growth zones	(2) Euhedral vein zones	(3) CL-gray veinlets or grain boundaries	(4) Intragranular variations	(5) Breccia boundaries	(6) CL-dark microfractures or grain boundaries
West of CF										
Pittsmont	3	11185-3771	BG	Qz-cp//EDM cut by qz-cp-py//NA	-	-	x	x	-	x
Pittsmont	4	11135-2470	BG	Qz-py-cp//PGS	x	x	-	-	-	-
Pittsmont	9	11135-2-4209	Steward ppy	Qz-mb//NA cut by barren qz//NA	x	-	x	x	-	-
Pervasive GS zone										
Central GS zone	12	10969R-2075	BG	Py-qz//GS	-	-	-	-	x	-
Central GS zone	13	10969-2101	BG	Py//GS cut by qz-mb-py//NA	-	x	-	-	-	-
Central GS zone	14	10969-2665	BG	Py-qz-op//GS cut by qz-mb-py//NA	-	-	-	-	x	-
Central GS zone	15	10969-5699	Aplite	Qz-mb//NA	-	-	-	x	-	x
Quartz vein stockwork										
Central	16	10969-6804	Aplite	Qz-mb//NA cut by barren qz//NA	-	x	x	-	-	x
Pittsmont	17	11135-5461	Aplite	Barren qz//NA	-	-	x	-	-	x
Shallow GS										
Anaconda	18	F2033-488	BG	Qz-py-cp//EDM	-	x	-	-	x	-
Anaconda	19	F2033-513	BG	Qz-mb//NA cut by qz-mb//NA	-	x	-	-	x	-
Pittsmont	20	11067-1	Modoc ppy	None	x	-	-	-	-	x
Pittsmont	26	11135-1150	BG	Qz-py-cp//EDM	-	-	-	-	x	-
East of CF										
Pittsmont	27	11172-1847	BG	Bi crackles cut by barren qz//NA	-	-	-	-	-	x
Pittsmont	30	BUR-03-214	BG	Qz-py//EDM	-	-	-	-	-	x

Notes: Map numbers correspond to sample labels on Figure 2; additional sample information can be found in Mercer and Reed (2013)
Abbreviations: BG = Butte Granite, CF = Continental fault, DH = drill hole, EDM = early dark micaceous, GS = gray sericitic, NA = no alteration, PGS = pale green sericitic; bi = biotite, cp = chalcopyrite, mb = molybdenite, op = open, ppy = porphyry, py = pyrite, qz = quartz

non-destructive, high-sensitivity spot analyses and another optimized for trace element mapping. Both setups were chosen to minimize sample damage and preserve the samples for additional analyses. We chose to measure Ti, Fe, K, and Al because these have been identified as CL active in quartz (Müller et al., 2003a; Landtwing and Pettke, 2005), and their concentrations are known from previous work to be unique within particular generations of magmatic and hydrothermal quartz (Rusk et al., 2006; Rusk et al., 2008a).

Spot analyses of quartz were acquired using a 15 keV accelerating potential, a 200 nA beam current, and a 20 μm spot size. Ti was measured simultaneously on two spectrometers with LPET and PET crystals, while Fe, K, and Al were measured on the remaining spectrometers. The "aggregate intensity" technique (Donovan et al., 2011) was applied to improve Ti counting statistics using Probe for Electron Microprobe Analyzer (EMPA) software. Ti, Fe, K, and Al were counted for 600 s on peak and 600 s off peak. Synthetic rutile was used as a Ti standard, synthetic magnetite was used for Fe, and natural orthoclase was used for K and Al. To reduce systematic continuum artifact errors, a matrix "blank" correction was applied to the Ti data using a synthetic quartz standard as a Ti-free blank (Donovan et al., 2011). Detection limits (99% confidence) achieved on spot analyses are 4 ppm for Ti, 12 ppm for Fe, 11 ppm for K, and 6 ppm for Al. We avoided analyzing quartz within 200 μm of rutile needles to avoid excitation of Ti atoms by Bremsstrahlung radiation and/or secondary fluorescence (e.g., Bastin et al., 1984; Wark and Watson, 2006; Llovet et al., 2012), and subsequent analyses of regions with erroneously high Ti concentrations in quartz contaminated by rutile were easily identified and eliminated. One-sigma analytical errors on individual Ti-in-quartz analyses range from 1.5% at high Ti concentrations (10s of ppm) to 10% at 16 ppm Ti. As Ti concentrations approach 0 ppm, the analytical errors grow exponentially with an error of ~50% at the detection limit of 4 ppm Ti.

High-sensitivity, low-resolution trace element mapping of one sample was carried out using a spectrometer setup similar to the spot analyses; however, counting times for Ti, Fe, K, and Al were reduced to 300 s on peak and 300 s off peak to reduce analysis time, resulting in a small loss of sensitivity. Despite this, mapping consumed ~70 h of instrument time. Detection limits (99% confidence) achieved on these maps are 7 ppm for Ti, 19 ppm for Fe, 13 ppm for K, and 9 ppm for Al, only slightly higher than for spot analyses. Maps were created by acquiring 20 μm spot analyses within a 120×680 μm rectangle that we interpolated with a kriging technique using Golden Software Surfer 8.0.

Ti-in-quartz temperatures

To carry out diffusion modeling, we used temperatures determined by Mercer and Reed (2013) specific for each sample, which are based on the Ti-in-quartz thermobarometer of Huang and Audétat (2012). The temperature calculations assumed a pressure of 250 MPa for porphyry quartz phenocrysts and vein quartz that formed near lithostatic pressure (early dark micaceous, barren quartz, and quartz-molybdenite), and 70 MPa for veins that formed near hydrostatic pressure (gray sericitic). Porphyry quartz grains do not contain primary, magmatic rutile, and thus we used an a_{TiO_2} of

0.5 for the porphyry quartz calculations based on analogy to similar silicic magma systems for which a_{TiO_2} was determined by equilibria among coexisting Fe-Ti oxides (e.g., Bishop Tuff; Wark et al., 2007) and the experimentally determined TiO_2 saturation model for rhyolite (Hayden and Watson, 2007). Primary, hydrothermal, blocky rutile occurs in all hydrothermal veins, so we used an a_{TiO_2} of 1.0 in all calculations for hydrothermal quartz. Assuming an a_{TiO_2} of 1.0 provides a minimum temperature estimate, whereas using an a_{TiO_2} of 0.5 yields a calculated temperature ~80°C higher. All quartz samples contain randomly oriented rutile "needles," which we infer grew by localized diffusion of Ti during subsequent cooling and exsolution (Cherniak et al., 2007), and we carefully avoided analyzing quartz within 200 μm of the rutile needles and associated radially cylindrical Ti depletion zones for spot analyses. Uncertainties in the calculated temperatures (i.e., due to pressure and a_{TiO_2} assumptions) could produce up to an order of magnitude shift in the calculated diffusive time scales, and we discuss this further below. A full discussion of the application of the Ti-in-quartz thermobarometer to these samples is provided in Mercer and Reed (2013). The focus of this work is on the calculation of time scales for processes leading to porphyry ore formation, rather than precise quantification of temperature variations.

SEM-CL brightness as a proxy for Ti concentration in quartz

The apparent CL image brightness is a function of operating conditions, such as carbon coat thickness, beam conditions, bias, and gain (Marshall, 1988; Götze et al., 2001). We kept these instrument variables nominally constant except for the beam current, which we had to change depending on the luminosity of the quartz (Rusk et al., 2006). For the following discussion, relative CL brightness is described as CL-black, CL-dark, CL-gray, and CL-bright.

Our analyses of trace element concentrations in relation to CL brightness described below show that brightness in the blue region correlates positively with Ti concentration, but is independent of other trace elements. This relationship has been previously demonstrated for igneous and high-temperature, porphyry-style hydrothermal quartz (e.g., Wark and Watson, 2006; Wark et al., 2007; Rusk et al., 2008a, 2011; Müller et al., 2010; Leeman et al., 2012). This enabled us to calibrate a subset of SEM-CL images with microprobe data so that the relative CL brightness could be attributed to known concentrations of Ti in quartz. Quantification of relative CL brightness profiles within each image was accomplished using the program ImageJ V 1.34s. Raw relative brightness profiles were smoothed using a 9-pixel averaged sliding bin. CL profiles were then calibrated for Ti using microprobe spot analysis profiles. Once we rigorously established this technique for several samples, we were able to calibrate additional CL profiles using relatively few microprobe analyses. This technique allowed us to take advantage of the high spatial resolution of CL images and minimized the need for costly microprobe trace element analyses.

Ti diffusion in quartz and time scales

Different generations of magmatic and hydrothermal quartz visible in CL images have distinct Ti concentrations and gradients, permitting modeling of Ti diffusion between

these quartz generations. In this study, an activation energy of 273 ± 12 kJ mol⁻¹ was assumed for diffusion parallel to the c-axis (001) in quartz (Cherniak et al., 2007). There is only limited anisotropy in the diffusion of Ti in quartz, and so it is not necessary to account for the orientation of the profile relative to the crystal (e.g., Ti diffusion in synthetic quartz at 800°C parallel to the c-axis is 3.75×10^{-21} m² s⁻¹, while that normal to the c-axis is 2.48×10^{-21} m² s⁻¹). Titanium diffusivity (D_{Ti}) is given by the Arrhenius relation:

$$D_{Ti} = 7 \times 10^{-8} * exp \left(\frac{-273 \pm 12\ kJ\ mol^{-1}}{RT} \right) m^2\ s^{-1}, \quad (1)$$

where R is the universal gas constant and T is the temperature in Kelvin, and has been experimentally calibrated for synthetic and natural quartz by Cherniak et al. (2007). The diffusivities used in this study are based on model temperatures selected from the results of Mercer and Reed (2013), and are summarized in Table 2. We obtain diffusion time scales by modeling diffusion as simple one-dimensional, concentration-independent diffusion in a semi-infinite medium (Carslaw and Jaeger, 1946) using the equation,

$$C(x,t) = c_{min} + \frac{(c_{max} - c_{min})}{2} * erfc \left(\frac{x}{2\sqrt{Dt}} \right), \quad (2)$$

where C is the concentration of Ti in quartz along a gradient between two distinct quartz generations with different Ti concentrations, x is the distance from the center of the gradient to the edge of the gradient, t is the time for diffusion, c_{min} and c_{max} are the minimum and maximum Ti concentrations, and D is the diffusivity of Ti in quartz. This method is similar to the one-dimensional approach employed by several workers modeling growth zones in igneous phenocrysts to obtain time

TABLE 2. Temperatures and Ti Diffusivities Used in Modeling

Model T(°C)[1]	Diffusivity, D (μm²/s)[2]
Experimentally determined, parallel to c-axis	
885	1.27×10^{-8}
750	8.24×10^{-10}
720	4.49×10^{-10}
690	2.44×10^{-10}
675	1.80×10^{-10}
670	1.63×10^{-10}
Extrapolated from experiments, parallel to c-axis	
645	9.82×10^{-11}
600	3.94×10^{-11}
585	2.91×10^{-11}
560	1.75×10^{-11}
520	7.80×10^{-12}
510	6.37×10^{-12}
505	5.75×10^{-12}
490	4.25×10^{-12}
485	3.84×10^{-12}
475	3.13×10^{-12}
470	2.83×10^{-12}
420	1.03×10^{-12}
400	6.85×10^{-13}

[1] Diffusion modeled at the maximum estimated temperature that any given quartz boundary may have experienced
[2] Diffusivities from the experiments of Cherniak et al. (2007)

scales of magmatic processes (e.g., Morgan et al., 2004; Wark et al., 2007; Matthews et al., 2012), and is the most straightforward approach for systems with rapid changes of temperature. The best-fit solutions to equation (2) were determined using the "lsqcurvefit" function in the MATLAB® Optimization Toolbox, which solves nonlinear data-fitting problems using a least-squares approach, to determine the best-fit time for most of the CL boundaries. Where obvious artifacts were present near CL boundaries, we estimated the best-fit time by eye to match the model with the artifact-free portion of the CL data.

Modeling the diffusion of Ti in quartz is based on several premises: First, Ti is the sole CL activator and thus differences in CL brightness are directly proportional to differences in the concentration of Ti in quartz. Second, all modeled CL boundaries were initially sharp and became diffuse over time at high temperature. The preceding premises are well supported by the findings reported below from microprobe and CL measurements. Third, we compute diffusion at a constant temperature. Diffusion is modeled at the maximum estimated temperature that any given quartz boundary may have experienced. For example, for a quartz phenocryst with a relatively Ti-poor, CL-gray core formed at ~690°C that was overgrown by Ti-rich, CL-bright quartz at 740°C (Fig. 3A), we assume the core-rim boundary experienced the hotter temperature, and thus we model the core-rim boundary at the temperature of the later quartz generation, 740°C. Alternatively, for a CL-bright, Ti-rich hydrothermal quartz vein formed at ~665°C that was cut by a CL-gray, Ti-poor 530°C quartz veinlet (Fig. 3C), we assume the first quartz had cooled to 530°C and we model diffusion at 530°C. Lastly, we do not take into account directly the ongoing diffusion of Ti as quartz cools below its formation temperature, during which time Ti diffusion slows until Ti gradients are essentially "frozen in," but we do examine the implications of this process. We describe 400°C as the effective closure temperature for this study, because below this temperature, there is no significant Ti diffusion on the ~1 m.y. time scale of interest for porphyry system formation. For example, at 400°C, an initially sharp Ti gradient will diffuse ~20 μm in 1 m.y., potentially producing boundaries we model, but below 400°C, boundaries on this length scale would take several tens of m.y. to form because diffusion is so slow. By using maximum temperatures, we calculate minimum time scales, representing the time from when the boundary formed until the quartz cooled below 400°C. The minimum diffusion times provide a starting point for exploring the likely actual time scales of porphyry magma residence, dike injections, stockwork vein formation, and cooling of the deposit.

Heat conduction profiles

We modeled the conduction of heat from injections of magma and hydrothermal fluids into cooler granitic host-rock to obtain a simple, first-order estimate for time scales of cooling. Heat conduction was modeled as simple one-dimensional, linear flow of heat in a semi-infinite medium (Carslaw and Jaeger, 1946). For simplicity, we ignored effects from magma and fluid flow rates, latent heat of crystallization, and viscosity (e.g., Delaney and Pollard, 1982; Rubin, 1995). We used two different models, one to simulate a single thermal event,
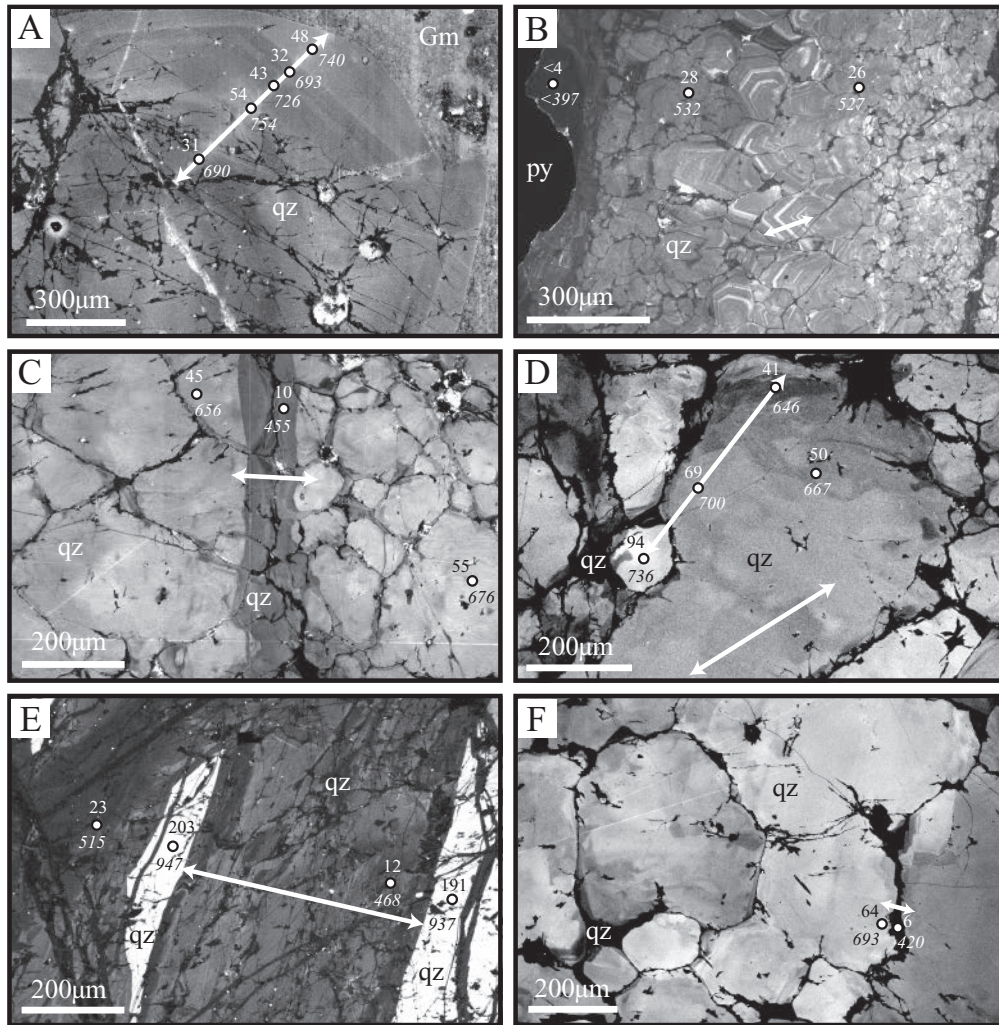
FIG. 3. Examples of cathodoluminescent textures in quartz. Quartz (qz) dominates these images unless otherwise marked: py = pyrite, Gm = groundmass. Representative microprobe analyses are shown with Ti concentrations given in ppm (above; regular font), and corresponding isobaric temperature estimates (°C) calculated using Huang and Audétat (2012; below, in italics). Arrows show examples of traverses across different quartz generations for which we modeled diffusion of Ti. (A) CL-bright porphyritic quartz "eye" from Steward porphyry dike with alternating CL-bright/CL-gray growth zones and microcracks filled with CL-black hydrothermal quartz (11135-2470_Q3). (B) Quartz-molybdenite-pyrite vein with euhedral growth zones (10969-2101_Q1). (C) CL-bright quartz-molybdenite vein cut by later stage CL-gray veinlet (11135-2-4209_ Q1). (D) Quartz-molybdenite vein with CL heterogeneity within and among quartz grains (10969-5699_Q2). (E) Angular fragments of CL-bright quartz from the Butte Granite cemented together by CL-dark quartz in a shallow gray sericitic vein (10969R-2075_Q1). (F) Barren quartz vein cut and surrounded by later stage CL-black quartz (11172-1847_Q3).

and one to simulate continuous thermal input. The first model simulates the conduction of heat from a single dike injection, or a single quartz vein-forming event, into a fracture in cooler granite host-rock using the equation:

$$T(x,t) = \left(\frac{T_{max} - \Delta T}{2}\right) * \left(erf\left(\frac{(x + x_i)}{2\sqrt{\kappa t}}\right) - erf\left(\frac{(x + x_i)}{2\sqrt{\kappa t}}\right)\right) \quad (3)$$

where T is the temperature in rock along a gradient between a hot dike or vein and cool host-rock, x is the distance from the center of the gradient to the edge of the gradient, x_i is the half width of the fracture, t is the time for conduction, T_{max} is the dike or vein temperature, ΔT is the temperature difference between the dike or vein and the host-rock, and κ is the thermal diffusivity in granite (6×10^5 μm²/s; Rubin, 1995).

Results from this model are dependent on the initial fracture aperture because this establishes the total thermal mass that is conserved as heat flows into the host-rock.

The second model simulates the conduction of heat during the gradual formation of a quartz vein by continuous input of fluids into a fracture of inconsequential width in cooler granite host-rock using the equation:

$$T(x,t) = T_g erf\left(\frac{|x|}{2\sqrt{\kappa t}}\right) + T_f erfc\left(\frac{|x|}{2\sqrt{\kappa t}}\right) \quad (4)$$

where T is the temperature in rock along a gradient from the edge of the fracture into the wall rock, x is the distance from the edge of the fracture to the edge of the gradient, t is the time for conduction, T_f is the temperature of the fluid, T_g is

the temperature of the host-rock, and κ is the thermal diffusivity of granite. The fracture width does not affect model results because the fluid continually supplies heat along the fracture edge regardless of fracture width.

Results

Quartz generations in SEM-CL

We investigated 15 samples including two porphyritic dikes, and more than a dozen stockwork veins (Table 1, Fig. 2) for their SEM-CL characteristics to identify different generations of magmatic and hydrothermal quartz precipitation. SEM-CL reveals six major quartz boundary types including (1) alternating CL-gray to CL-bright porphyry phenocryst growth zones (Fig. 3A), (2) alternating CL-bright/gray euhedral growth zones in veins (Fig. 3B), (3) CL-gray veinlets or grain boundaries that appear to cut CL-bright vein quartz grains (Fig. 3C), (4) intragranular variations within grains of primary vein quartz (Fig. 3D), (5) brecciated CL-bright host-rock quartz cemented by CL-dark hydrothermal quartz (Fig. 3E), and (6) narrow (5–20 μm) microfractures and grain boundaries in vein quartz filled with CL-black quartz (Fig. 3F).

Correlation of trace elements with SEM-CL brightness

Trace element concentration profiles and spot analyses were acquired for all samples and incorporate different generations of magmatic and hydrothermal quartz. We compared trace element profiles to relative CL brightness to determine whether trace element concentrations correlate with quartz generations of distinct brightness (Fig. 4). Ti concentrations range from below the detection limit of 4 ppm to as high as 50 ppm, Al ranges from 50 to 1,600 ppm, Fe ranges from 20 to 700 ppm, and K ranges from below the detection limit of 11 ppm to 260 ppm. Concentrations of Al, Fe, and K do not correlate with CL brightness. Some Al and K concentrations parallel each other, likely owing to their coupled substitution for Si or to contamination from microinclusions of K-Al silicate minerals (sericite, K-feldspar). Low concentrations of Ti correlate with CL-dark to -gray quartz while higher Ti concentrations correlate with CL-bright quartz. For example, the CL-gray core of the porphyry quartz phenocryst (Fig. 4A) is Ti-poor as are the CL-black hydrothermal veinlets (Fig. 4B), while CL-bright growth bands in the quartz phenocryst and CL-bright hydrothermal vein quartz are relatively Ti rich. Detailed quantitative CL brightness profiles mimic electron microprobe Ti traverses (Fig. 4), further demonstrating their positive correlation.

While the correlation between Ti concentration and CL brightness is clear for the samples shown in Figure 4, this was less apparent for many other samples owing to complications with image quality caused by CL-bright scratches and CL-black cracks, and contamination of data by inclusions of rutile, sericite, and K-feldspar. To examine these effects over a larger area we acquired a high-sensitivity trace element map over a 120 × 680 μm swath for a crosscutting hydrothermal vein (Fig. 5).

High concentrations of trace elements in Figure 5 are shown in warm colors (red, yellow, green) while low concentrations appear in cool colors (blue, violet, pink). Dark purple areas are below the 99% minimum detection limit (MDL = pink). The Ti map shows a clear correlation between Ti concentration and CL brightness within the 20-μm map resolution. Three spots of unusually high Ti concentrations are tiny rutile needles (<1 × 20 μm) within the quartz. A slight mismatch between the edges of CL features and Ti map concentrations can be attributed to repolishing the sample between SEM-CL imaging and microprobe mapping, which likely moved boundaries by several μm. Maps of Al, Fe, and K show that the concentrations of these elements do not correspond to CL features. However, patterns on the Al and K maps approximately match each other, again supporting the hypothesis that they either participate in coupled substitution for Si or that there is contamination from microinclusions of K-Al silicate minerals. The map of Fe concentration shows that Fe does not correlate with Ti, Al, or K in quartz. Spots of high concentrations of Al, K, and Fe are likely tiny mineral inclusions of sericite, K-feldspar, or Fe oxides.

Modeling of Ti diffusion in quartz

By modeling the diffusion of Ti in quartz we can constrain the time scales over which initially sharp CL boundaries between quartz generations become diffuse. We selected CL boundaries from the calibrated, smoothed CL brightness profiles, ensuring that boundaries were representative of a meaningful transition between quartz generations rather than image noise (e.g., scratches, cracks). Examples of modeling results for four different CL boundaries from each sample are shown for a porphyry quartz phenocryst (Fig. 6A; profiles A, B, C, and D) and a CL-bright hydrothermal barren quartz vein that is cut by CL-dark veinlets (Fig. 6B; profiles A, A', B, and B'). CL boundaries, shown with thick black lines, are modeled by iteratively solving equation (2) until the modeled Ti gradient most closely matches that defined by the CL image brightness profile. Bounding model results are shown with thin gray curves and corresponding time scales are reported in years. Red curves and corresponding time scales represent best-fit model results for each boundary. Best-fit time scales have an estimated uncertainty of ≤10%.

Time scales for diffusion of Ti between growth rim boundaries in the porphyry quartz phenocryst (Fig. 6A) range from as long as 6,000 years to as short as 50 years, decreasing from core to rim. This decreasing progression in time scales probably results from the phenocryst core having spent more integrated time at elevated temperatures than did successive phenocryst rims, allowing more Ti diffusion along the core boundary. The core boundary provides an estimate of 6,000 years for porphyry magma residence, i.e., the time from quartz core growth within a crustal magma reservoir to magma injection as a porphyry dike and cooling below 400°C. The outer rim boundary provides an estimate of 50 years for the time from phenocryst rim growth to porphyry dike injection and cooling below 400°C. Not all boundaries visible in the CL image were modeled because many had Ti concentration differences that were too small to confidently distinguish from background image noise.

Diffusion modeling of the hydrothermal quartz veinlets (Fig. 6B) results in time scales ranging from 23,000 to 60,000 years, representing the time from when the CL-dark veinlets cut the CL-bright vein until the time when the veins cooled below 400°C. Boundaries from both sides of the same veinlets are different by 27,000 to 34,000 years, which we
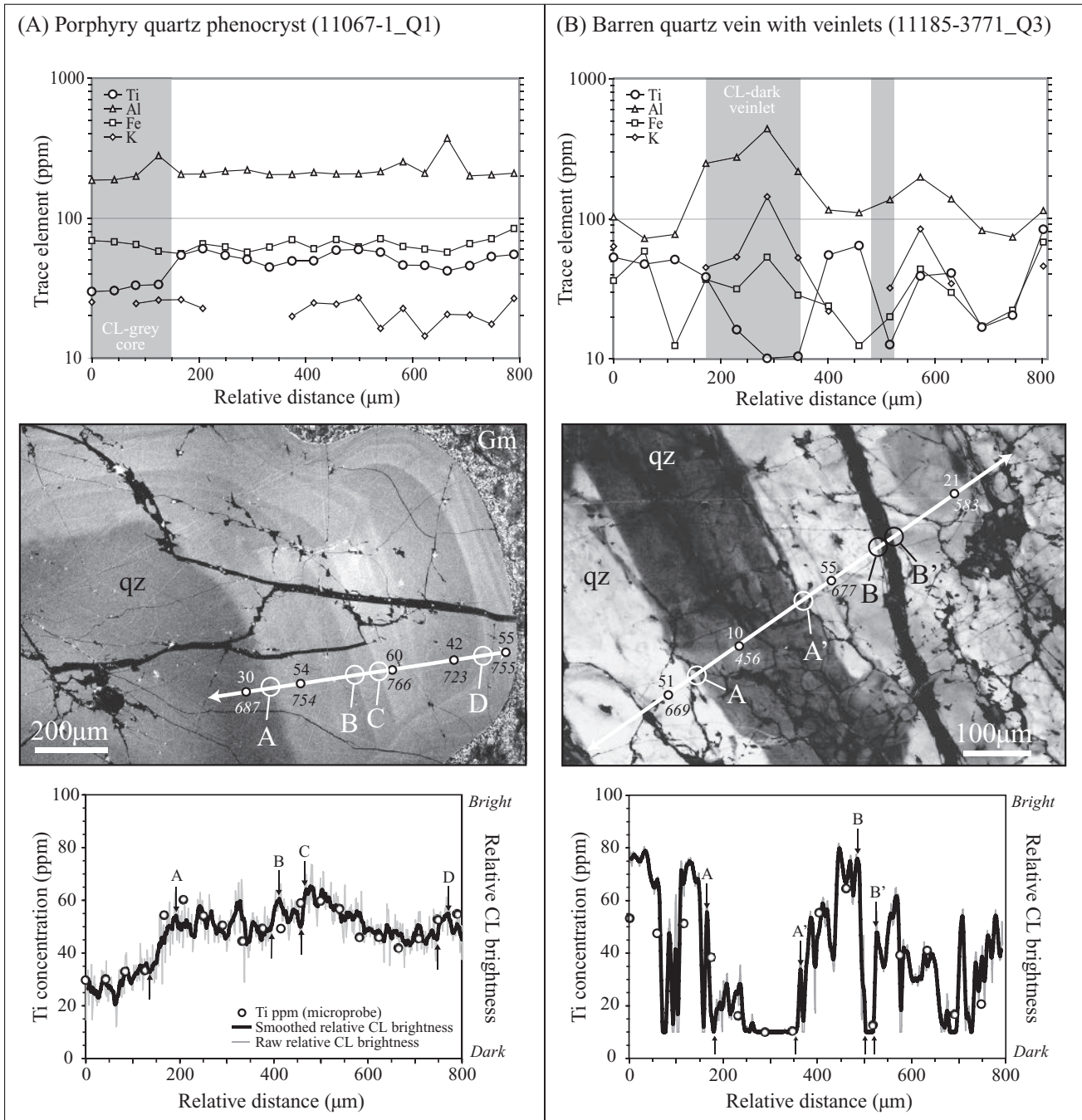
FIG. 4. Examples of microprobe trace element traverses (top), corresponding SEM-CL images (middle), and SEM-CL brightness calibration (bottom) for (A) CL-bright porphyritic quartz "eye" from Modoc porphyry dike with CL-dark core and prominent microcracks filled with CL-black hydrothermal quartz (11067-1_Q1) and (B) CL-bright barren quartz vein with crosscutting CL-dark veinlets (11185-3771_Q3). Data points missing on the trace element traverses are analyses that are below the 99% minimum detection limit. Arrows in SEM-CL images indicate location of microprobe and CL traverses. Letters along traverses (A, B, C, D, A', B') denote representative boundaries chosen for modeling. Representative microprobe analyses are shown with Ti concentrations given in ppm (regular font), and corresponding isobaric temperature estimates in °C (italics) calculated using Huang and Audétat (2012). Raw CL intensity profiles are shown in gray, smoothed CL intensity profiles are shown in black, and Ti analyses used to calibrate CL brightness profiles are shown with circles.

attribute to the complexity of CL features near the boundary of the veinlets that affect the shape of CL brightness profiles.

A drawback to our procedures for quantifying time scales is that we may bias the results toward the shorter time scales corresponding to features that are easier to identify and model. For example, we cannot characterize time scales for CL features that may have existed but diffused to the point that they are now indistinguishable in CL images. However, this problem is likely unimportant because features that are clearly primary (e.g., crosscutting veins, euhedral growth zones in veins)
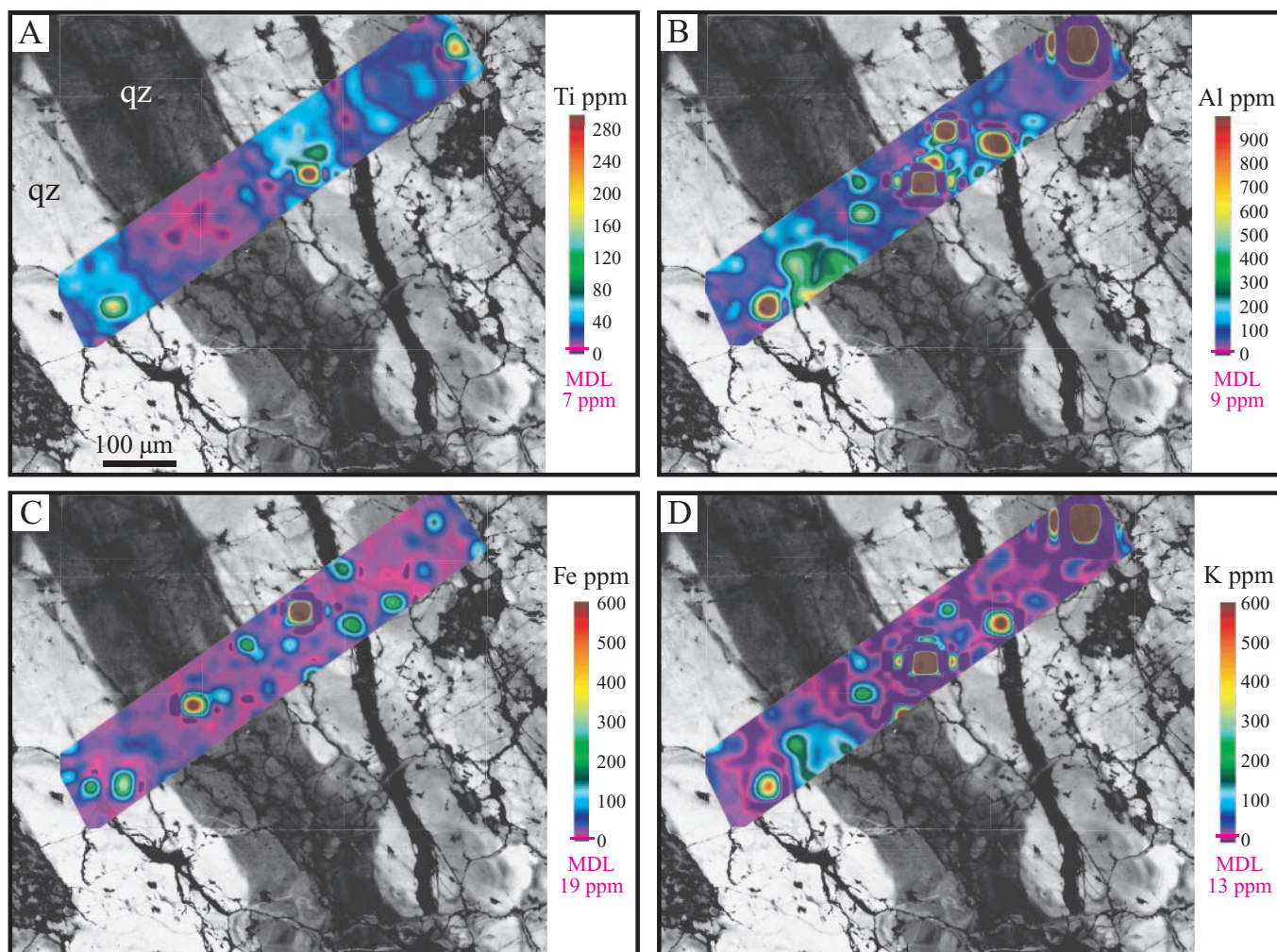
FIG. 5. Microprobe trace element maps in CL-bright barren quartz vein that is cut by CL-dark veinlets (11185-3771_Q3). Map created by interpolating 20 μm spot analyses within a 120 × 680 μm rectangle. High concentrations of trace elements are shown in warm colors (red, yellow, green) while low concentrations appear in cool colors (blue, violet, pink). Dark purple areas are below the 99% minimum detection limit (MDL; pink). (A) Ti concentration in quartz correlates positively with CL brightness. Three spots of high Ti concentrations surround inclusions of rutile needles. (B) Al concentrations, (C) Fe concentrations, and (D) K concentrations do not correlate with CL brightness. Al and K show a moderate correlation due either to coupled substitution for Si or to contamination from microinclusions of K-Al silicate minerals. Spots of high (i.e., ~100s of ppm) concentrations of Al, K, and Fe are likely tiny mineral inclusions of sericite, K-feldspar, or Fe oxides.

and old (e.g., phenocryst growth zones) are preserved and easily identified in these samples. Samples from deep within the deposit (e.g., Fig. 2, map numbers 9, 15, 16, and 17), where the overall vein density is higher (Reed et al., 2013), dominantly exhibit mottled to monotonous textures that could initially be interpreted as quartz that "lost" textures during pervasive heating and diffusion. However, these textures coexist with a small proportion of distinctly zoned features (e.g., euhedral oscillatory zones) in what appears to be the same generation of quartz (Mercer and Reed, 2013). This observation leads us to conclude that the mottled to monotonous textures are original textures, perhaps owing to a particular growth process at depth that precludes sharp growth zones, e.g., crystallization from an originally amorphous or cryptocrystalline mass due to a large pressure drop. Although the effect of vein depth and density on diffusive time scales merits further study, we think it unlikely that there was an entire generation of older

features that diffused away while the features we clearly see were preserved. Thus the time scales we present here provide a practical estimate of porphyry formation processes.

We modeled 83 different CL boundaries spanning all six quartz boundary types within these 15 samples. A summary of model time scale results as a function of assumed temperature is tabulated in Table 3 and Figure 7. "Isodiffusion lines" represent equal Ti gradient steepness, or equivalently, CL boundary sharpness, which we quantify by calculating the best-fit model to a particular CL boundary at temperatures selected from the results of Mercer and Reed (2013). Boundaries with steep Ti gradients plot toward the "sharp" isodiffusion line, corresponding to shorter time scales for a given diffusion temperature, while boundaries with gentler Ti gradients plot toward the "diffuse" isodiffusion line, corresponding to longer time scales. The sharpest boundary we modeled displays modified Ti concentrations over ~2 μm while the most diffuse
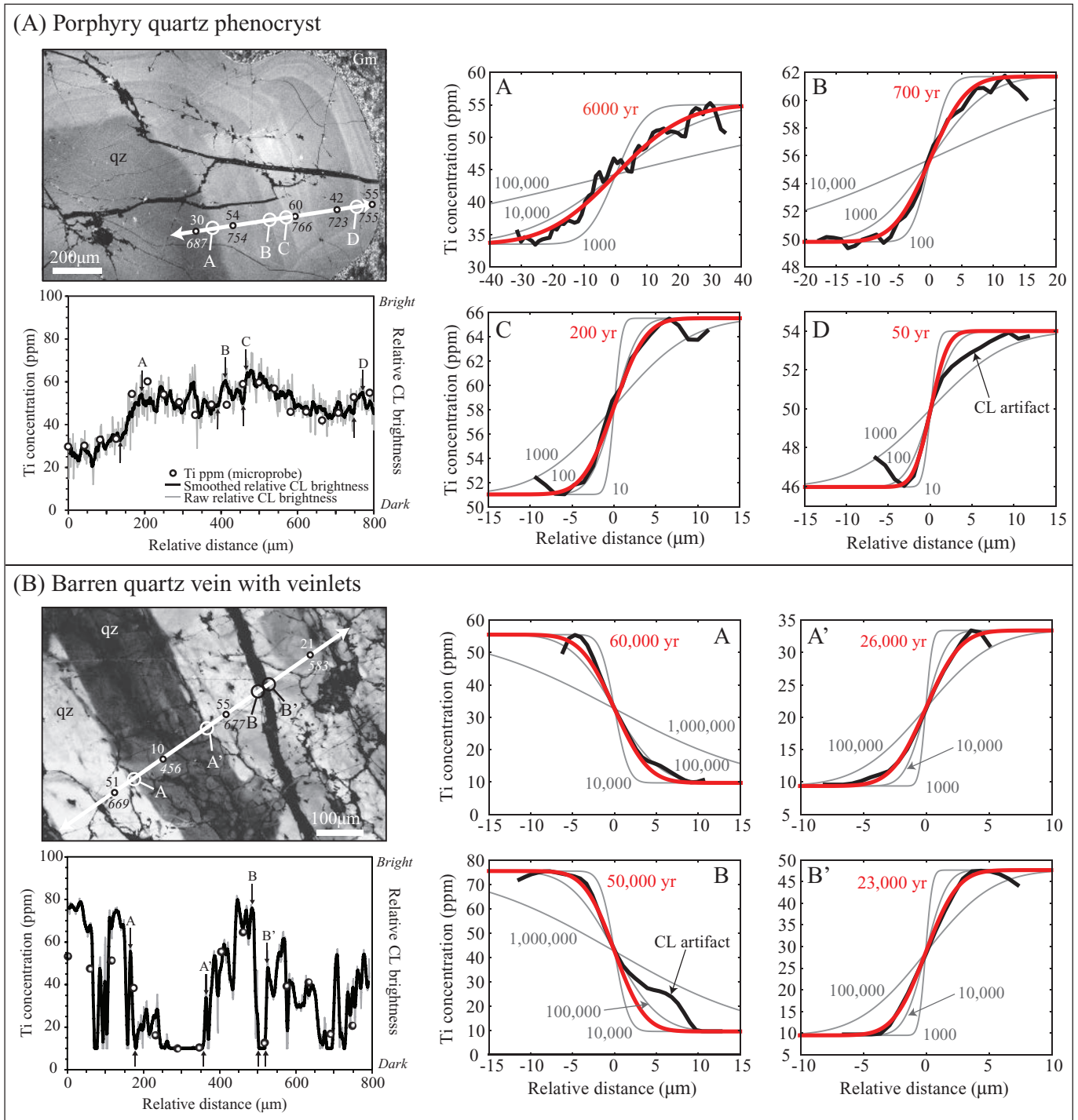
FIG. 6. Examples of modeling Ti diffusion in quartz from (A) porphyry quartz phenocryst (11067-1_Q1) and (B) CL-bright barren quartz vein with crosscutting CL-dark veinlets (11185-3771_Q3). Calibrated CL intensity profiles are shown in black and bounding model results are shown with thin gray curves and corresponding time scales reported in years. Red curves and corresponding time scales represent best-fit model results for each profile. Artifacts near CL boundaries are ignored during modeling (e.g., profile D). Best-fit time scales have an estimated uncertainty of ≤10%. Note the different scales on the models.

boundary displays modification over ~100 μm. Euhedral vein zones, breccia boundaries, and CL-black microfractures and grain boundaries typically display steeper Ti gradients while phenocryst growth zones, CL-gray veinlets or grain boundaries, and intragranular variations show both sharp and more diffuse boundaries. Diffusion time scales for porphyry quartz phenocryst formation and cooling range from 50 to 6,000 years, while those for hydrothermal vein formation, refilling, and cooling range from 10 to 60,000 years. Though there is a considerable spread of modeled time scales of diffusion,

TABLE 3. Summary of Ti Diffusion Modeling

Quartz boundary type	Model T range (°C)	Best-fit time range (years)
Phenocryst growth zones	720–750	50–6,000
Euhedral vein zones	475–720	10–20,000
CL-gray veinlets or grain boundaries	400–470	700–60,000
Intragranular variations	645–675	400–50,000
Breccia boundaries	485–585	400–20,000
CL-black microfractures or grain boundaries	475–690	300–60,000

results are generally several orders of magnitude shorter than the estimated ~0.6 m.y. duration for each pulse of pre-Main stage porphyry mineralization (Fig. 7).

Modeling of heat conduction for dikes and veins

Time scales for the conduction of heat away from dike injections and veins (Fig. 8) provide a reference point to compare Ti diffusion time scales and an estimate of how long the dikes and veins might stay hot enough to allow Ti diffusion. Modeling injection of a single 5 m dike injection at 750°C into granite host rock that is 400°C (Mercer and Reed, 2013) illustrates that porphyry dikes would cool to 400°C on time scales of 10 s to 100 years (Fig. 8A, left). A 1-cm-wide fracture with a single injection of 600°C fluids would cool on time scales of minutes to hours (Fig. 8A, right). Modeling a short duration of fluid flow in a fracture may be appropriate for quartz veins without alteration envelopes (such as the Butte quartz-molybdenite veins) that apparently formed by episodic, adiabatic fluid
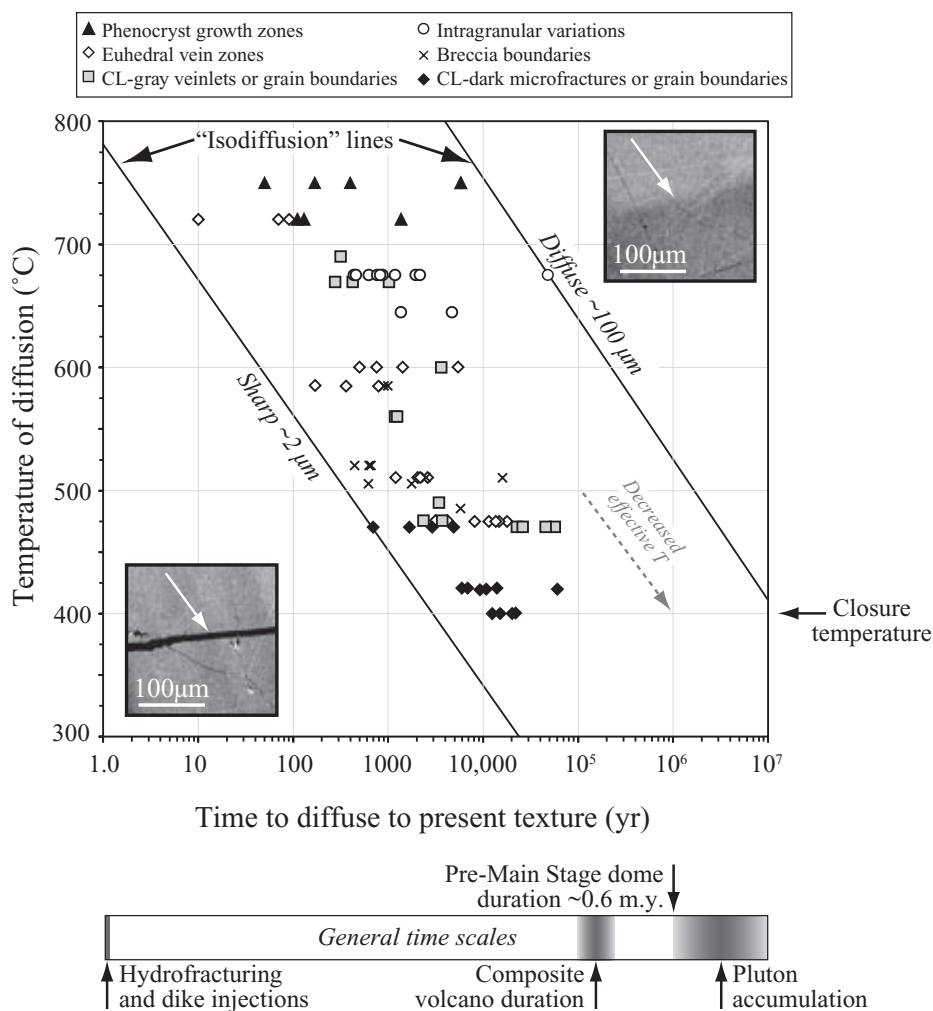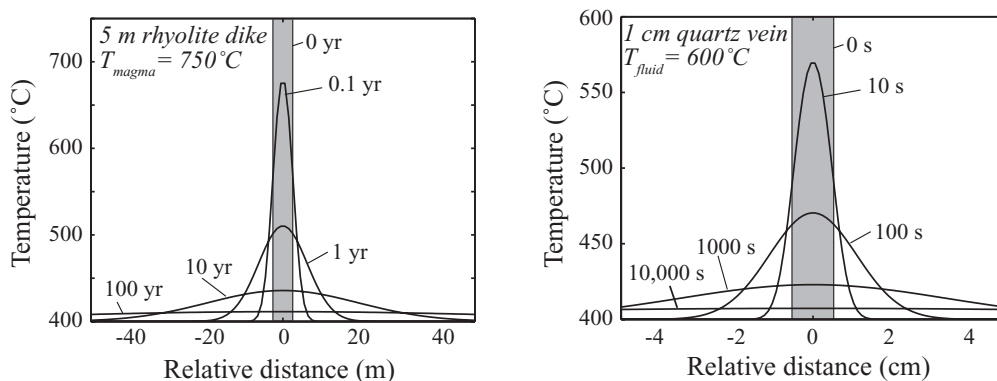

FIG. 7. Summary of modeled time scales as a function of assumed model temperature. "Isodiffusion" lines represent lines of equal Ti gradient steepness, or CL boundary sharpness, and are computed by calculating best-fit models to particular CL boundaries at different temperatures. The sharpest boundary we modeled displays modified Ti concentrations over ~2 μm while the most diffuse boundary displays modification over ~100 μm. Gray dashed arrow shows how a 100°C decrease in effective model temperature moves a modeled boundary along its isotexture line to nearly an order of magnitude longer calculated time scale. Duration of each pulse of pre-Main stage porphyry formation at Butte is estimated to be ~0.6 m.y. by radiogenic isotopes (Lund et al., 2002, 2005; Dilles et al., 2003). General time scales of magmatic and hydrothermal processes are shown with shaded bars at the bottom, matched to the times on the x-axis of the graph. Time scales for the formation of 2 km long hydrofractures and silicic dikes are on the order of minutes to hours, respectively (assuming a hydrofracturing rate of ~1 m/s (Bons, 2001) and a dike injection rate of ~0.015 m/s (Rutherford and Gardner, 2000)). Duration of average composite volcanoes ranges from 100 to 250 kyr (Davidson and De Silva, 2000) and plutons accumulate over 1 to 10 m.y. (Glazner et al., 2004).

(A) Heat conduction from single injection of magma or hydrothermal fluid into 400°C granitic host rock

(B) Heat conduction from continuous flow of hydrothermal fluid into 400°C granitic host rock
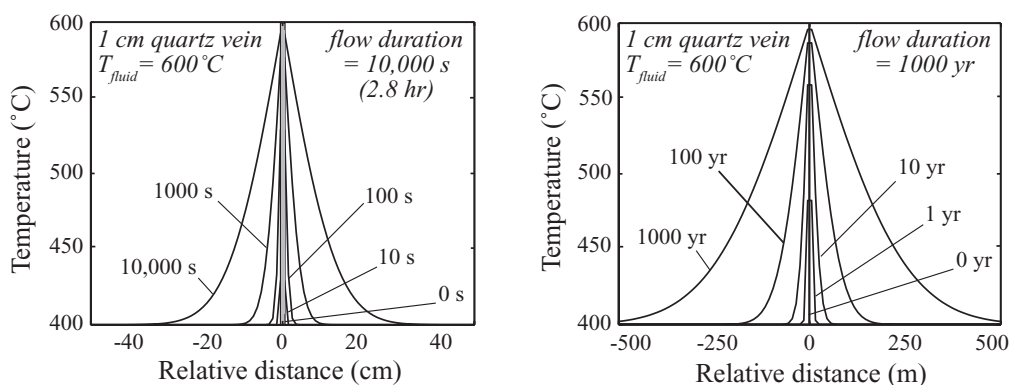

FIG. 8. Model results for conduction of heat from injections of magma or hydrothermal fluid into 400°C granitic host rock. Model uses thermal diffusivity for granite, $\kappa = 6 \times 10^5 \ \mu m^2/s$. (A) Temperature profiles illustrate the conduction of heat from a single thermal event: (Left) single injection of 5 m rhyolitic dike at 750°C cools to 510°C in 1 year and cools to near host rock temperature in 100 years. Over 100 years, the dike heats >100 m of wall rock to ~410°C; (Right) one-cm fracture filled once with 600°C fluid cools to 470°C in 100 s and cools to near host rock temperature in 10,000 s (~2.8 h). Over 10,000 s the vein heats >10 cm of wall rock to ~410°C. (B) Temperature profiles show the conduction of heat from continuous thermal input: (Left) fracture of inconsequential width filled continuously with 600°C fluid for 10,000 s (2.8 h). After 10,000 s, the fluid heats ~40 cm of wall rock to 470°C; (Right) fracture of inconsequential width filled continuously with 600°C fluid over a much longer duration of 1,000 years. After 1,000 years, the fluid heats ~400 cm of wall rock to 470°C. Note the different relative distances and time scales of the models.

decompression, while modeling vein formation with continuous fluid flow may be more appropriate for quartz veins with cm-scale alteration envelopes that apparently formed by pressure drop, temperature drop, and wall-rock reaction (Rusk and Reed, 2002; Rusk et al., 2008b; Reed et al., 2013). Formation of a 1 cm vein by gradual crystallization from continuous input of fluids at 600°C over short time scales of minutes to hours heats more wall rock than the previous case. For example, after 10,000 s (2.8 hr) of fluid flow, wall rock is heated to 500°C at ~10 cm away from the fracture (Fig. 8B, left). Formation of a 1 cm quartz vein by continuous fluid input over longer time scales of 10s of years to 1,000 years heats a larger amount of wall rock. After 1,000 years of fluid flow, the wall rock is heated to 500°C ~200 m away from the fracture (Fig. 8B, right). The long time scales in the last case may not apply to vein stockworks because if each stockwork vein heated up a large volume of rock, the host-rock could increase in temperature by 100s of °C. However, there is no evidence for pervasive heating of wall rock to temperatures above the granite solidus (~700°C) at Butte (Roberts, 1975).

Discussion

Ti as the primary SEM-CL activator in magmatic and hydrothermal quartz

Several elements, including H, Li, Na, Al, K, Ti, Cr, Mn, Fe, Eu, and Pb, are known to be CL activators in quartz from various geologic settings (e.g., Watt et al., 1997; Götze et al., 2001; Penniston-Doreland, 2001; Müller et al., 2003a, b, 2010; Landtwing and Pettke, 2005; Rusk et al., 2006, 2008a, 2011; Lehmann et al., 2009; Götte et al., 2011; Leeman et al., 2012). Ti has been shown to be the principal CL activator in the blue region (~440–460 nm) in igneous quartz (D'lemos et al., 1997; Götze et al., 2001; Müller et al., 2003a; Wark and Watson, 2006; Wark et al., 2007; Betsi et al., 2010; Leeman et al., 2012) and in high-temperature (>400°C) hydrothermal quartz (Rusk et al., 2006, 2008a, 2011; Müller et al., 2010; Götte et al., 2011; Rusk, 2012). The positive correlation between Ti concentration and blue CL brightness in magmatic and high-temperature stockwork vein quartz that we describe in this study agrees well with previous work. The findings cited above—the

striking correlation of Ti concentrations with blue CL brightness in both microprobe traverses (Fig. 4) and the map (Fig. 5), and the lack of correlation with the other trace elements in the quartz—demonstrate that Ti is the primary CL activator. This correlation, along with the recent calibration of the Ti-in-quartz thermobarometer (Huang and Audétat, 2012) and calibrated diffusivity of Ti in quartz (Cherniak et al., 2007) makes diffusion modeling a robust and powerful tool for studies of igneous and hydrothermal quartz forming processes.

Time scales of porphyry deposit formation and cooling

We interpret the modeled Ti diffusion time scales as the total time from quartz boundary formation to the time when temperatures dropped below 400°C, the effective closure temperature. This time frame does not require constant high-temperature exposure; it could also represent a summation of discrete, short heating events. For example, the time could incorporate Ti diffusion during the initial high temperature just after boundary formation as well as Ti diffusion during reheating events due to subsequent magma or hydrothermal fluid injections nearby. Our technique cannot distinguish between these possibilities, thus we discuss the time scales as the total time juxtaposed generations of quartz spent at elevated temperature.

Interpretation of the diffusion data depends on temperature assumptions in our simple model and an evaluation of time-integrated cooling by considering its effect on time scales of diffusion. The Ti diffusion boundaries are defined by their Ti gradient steepness, or CL sharpness, regardless of temperature, so each boundary is confined to its own isodiffusion line—the line of equal Ti gradient steepness or CL sharpness that passes through a modeled point—parallel to the "sharp" and "diffuse" isodiffusion lines shown in Figure 7. The cooling of any diffusion boundary has the effect of sliding any given point down its isodiffusion line toward lower effective model temperatures and longer time scales, as shown in Figure 7 by the gray dashed arrow. For example, if the actual dominant diffusion temperature were 100°C cooler than the temperature where a given point is plotted in Figure 7, calculated time scales would be nearly an order of magnitude longer.

Single hydrofracturing fluid injections likely extend at least 2 km vertically at Butte, as indicated by biotite crackles that reach >2 km from the deep fluid source, and would take approximately 30 minutes to propagate, assuming a rate of ~1 m/s (Bons, 2001). Porphyry dikes extend at least 2 km vertically and dike injections would take approximately one to two days, assuming a rhyolitic dike propagation rate of ~0.015 m/s (Rutherford and Gardner, 2000). Fragments in biotite breccias along the contact of porphyry dikes are matrix supported, indicating rapid quenching. Considering that rhyolite dikes would likely take tens of years to cool once emplaced (Fig. 8A), the time scales we find for the formation and cooling of porphyry quartz phenocryst rims, ~50 years (Fig. 7), seems reasonable. Wark et al. (2007) investigated Ti-concentration profiles for quartz phenocrysts rims from the Bishop Tuff and found that phenocrysts rims formed within 100 years of the 0.76 Ma eruption that produced the Bishop Tuff, similar to the time scales we calculate here.

Fluid flow rates and flow duration during vein formation are not known, and estimates of time scales for vein cooling from thermal models vary widely, from seconds to 100s of years (Fig. 8B-D) depending on assumptions about fluid flow duration. At any given temperature, we find widely varying time scales for diffusion between adjacent hydrothermal quartz generations (Fig. 7), perhaps indicating a wide spectrum of fluid flow duration. Modeling of reactive transport in sericitic alteration envelopes (Geiger et al., 2002) suggests that cm-scale envelopes could form in <100 years at 400°C. For envelope-bearing veins, 600°C fluids could heat the surrounding rock up to 500°C several 10s of m away from the fracture (Fig. 8D), which could insulate the vein, allowing prolonged diffusion of Ti until the whole mass of rock cooled below 400°C. However, the most diffuse boundaries (30-100 μm wide) occur in higher temperature (>600°C) quartz only (Fig. 7), suggesting that the high temperatures needed for such diffusion did not last long, and that time scales to produce the most diffuse boundaries at lower temperatures like ~500°C did not occur; i.e., for veins that form at 500°C, the rock typically cools from 500°C to less than 400°C so fast that diffuse CL boundaries do not form. The abundance of relatively sharp CL boundaries (Fig. 7) indicates that in many cases vein quartz cooled relatively quickly, in 10s to 10,000s of years, otherwise all boundaries we observe in the quartz veins would be diffuse, regardless of the temperature estimate.

Conclusions

Our SEM-CL and microprobe findings contribute to the growing evidence that Ti is a consistent CL activator in high-temperature magmatic and hydrothermal quartz. We use this correlation to calibrate SEM-CL images with Ti concentrations obtained by high-sensitivity electron microprobe analyses, enabling us to model the time scales for diffusion of Ti between distinct generations of magmatic and hydrothermal quartz. We conclude that individual porphyry dikes and hydrothermal veins may reasonably cool on time scales of 10s to 10,000s of years, which is significantly shorter than the ~0.6 m.y. time span of porphyry mineralization pulses at Butte indicated by radiogenic isotopes. Our Ti diffusion results show that porphyry Cu deposits likely form by short-lived magmatic and hydrothermal injections, each creating its own thermal spike, that repeat over a span of a few m.y. to form a porphyry deposit such as the Butte pre-Main stage.

manuscript. Any use of trade, product, or firm names is for descriptive purposes only and does not imply endorsement by the U.S. government.

REFERENCES

Bastin, G.F., Loo, F.J.J., Vosters, P.J.C., and Vrolijk, J.W.G.A., 1984, An iterative procedure for the correction of secondary fluorescence effects in electron-probe microanalysis near phase boundaries: Spectrochimica Acta, v. 39, p. 1517–1522.

Betsi, T.B., and Lentz, D.R., 2010, The nature of "quartz eyes" hosted by dykes associated with Au-Bi-As-Cu, Mo-Cu, and Base-metal-Au-Ag mineral occurrences in the Mountain Freegold region (Dawson Range), Yukon, Canada: Journal of Geosciences, v. 55, p. 347–368.

Bons, P.D., 2001, The formation of large quartz veins by rapid ascent of fluids in mobile hydrofractures: Tectonophysics, v. 336, p. 1–17.

Brimhall, G.H., 1973, Mineralogy, texture, and chemistry of early wall rock alteration in the deep underground mines and continental area, Butte District, Montana: Butte Field Meeting of Society of Economic Geologists, p. H1-H5.

Burnham, C.W., 1979, Magmas and hydrothermal fluids, in Barnes, H.L., ed., Geochemistry of hydrothermal ore deposits, 2nd ed.: New York, John Wiley, p. 71–136.

Candela, P.A., and Piccoli, P.M., 2005, Magmatic processes in the development of porphyry-type ore systems: ECONOMIC GEOLOGY 100TH ANNIVERSARY VOLUME, p. 25–37.

Carslaw, H.S., and Jaeger, J.C., 1946, Linear flow of heat: The infinite and semi-infinite solid, Conduction of Heat in Solids: London, Oxford University Press, 383 p.

Cathles, L.M., and Shannon, R., 2007, How potassium silicate alteration suggests the formation of porphyry ore deposits begins with the nearly explosive but barren expulsion of large volumes of magmatic water: Earth and Planetary Science Letters, v. 262, p. 92–108.

Cherniak, D.J., Watson, E.B., and Wark, D.A., 2007, Ti diffusion in quartz: Chemical Geology, v. 236, p. 65–74.

Cline, J.S., and Bodnar, R.J., 1991, Can economic porphyry copper mineralization be generated by a typical calc-alkaline melt?: Journal of Geophysical Research, v. 96, p. 8113–8126.

Cloos, M., 2001, Bubbling magma chambers, cupolas, and porphyry copper deposits: International Geology Review, v. 43, p. 285–311.

Cooke, D.R., Hollings, P., and Walshe, J.L., 2005, Giant porphyry deposits: Characteristics, distribution, and tectonic controls: ECONOMIC GEOLOGY, v. 100, p. 801–818.

Costa, F., Dohmen, R., and Chakraborty, S., 2008, Time scales of magmatic processes from modeling the zoning patterns of crystals: Reviews in Mineralogy and Geochemistry, v. 69, p. 545–594.

Davidson, J., and De Silva, S., 2000, Composite Volcanoes, in Sigurdsson, H., ed., Encyclopedia of Volcanoes, Academic Press, p. 663–681.

Delaney, P.T., and Pollard, D.D., 1982, Solidification of basaltic magma during flow in a dike: American Journal of Science, v. 282, p. 856–885.

Dilles, J.H., 1987, Petrology of the Yerington Batholith, Nevada: Evidence for evolution of porphyry copper ore fluids: ECONOMIC GEOLOGY, v. 82, p. 1750–1789.

Dilles, J.H., and Einaudi, M.T., 1992, Wall-rock alteration and hydrothermal flow paths about the Ann-Mason porphyry copper deposit, Nevada: A 6 km vertical reconstruction: ECONOMIC GEOLOGY, v. 87, p. 1963–2001.

Dilles, J.H., Martin, M.W., Stein, H., and Rusk, B.G., 2003, Re-Os and U-Pb ages for the Butte copper district, Montana; A short- or long-lived hydrothermal system?: Geological Society of America Abstract with Programs, v. 35, p. 400.

D'lemos, R.S., Kearsley, A.T., Pembroke, J.W., Watt, G.R., and Wright, P., 1997, Complex quartz growth histories in granite revealed by scanning cathodoluminescence techniques: Geological Magazine, v. 134, p. 549–552.

Donovan, J.J., Lowers, H.A., and Rusk, B.G., 2011, Improved electron probe microanalysis of trace elements in quartz: American Mineralogist, v. 96, p. 274–282.

Du Bray, E.A., Aleinikoff, J.N., and Lund, K., 2012, Synthesis of petrographic, geochemical, and isotopic data for the Boulder Batholith, southwest Montana: U.S. Geological Survey Professional Paper 1793, 39 p.

Geiger, S., Haggerty, R., Dilles, J., Reed, M.H., and Matthai, S., 2002, New insights from reactive transport modeling: The formation of sericitic vein envelopes during early hydrothermal alteration at Butte, Montana: Geofluids, v. 2, p. 185–201.

Glazner, A.F., Bartley, J.M., Coleman, D.S., Gray, W., and Taylor, R.Z., 2004, Are plutons assembled over millions of years by amalgamation from small magma chambers?: GSA Today, v. 14, p. 4–11.

Götte, T., Pettke, T., Ramseyer, K., Koch-Müller, M., and Mullis, J., 2011, Cathodoluminescence properties and trace element signature of hydrothermal quartz: A fingerprint of growth dynamics: American Mineralogist, v. 96, p. 802–813.

Götze, J., Plötze, M., and Habermann, D., 2001, Origin, spectral characteristics and practical applications of the cathodoluminescence (CL) of quartz: A review: Mineralogy and Petrology, v. 71, p. 225–250.

Guillou-Frottier, L., and Burov, E., 2003, The development and fracturing of plutonic apexes: Implications for porphyry ore deposits: Earth and Planetary Science Letters, v. 214, p. 341–356.

Hayden, L.A., and Watson, E.B., 2007, Rutile saturation in hydrous siliceous melts and its bearing on Ti-thermometry of quartz and zircon: Earth and Planetary Science Letters, v. 258, p. 561–568.

Huang, R., and Audétat, A., 2012, The titanium-in-quartz (TitaniQ) thermobarometer: A critical examination and re-calibration: Geochimica et Cosmochimica Acta, doi:10.1016/j.gca.2012.01.009.

Landtwing, M.R., and Pettke, T., 2005, Relationships between SEM-cathodoluminescence response and trace-element compositions of hydrothermal vein quartz: American Mineralogist, v. 90, p. 122–131.

Landtwing, M.R., Pettke, T., Halter, W.E., Heinrich, C.A., Redmond, P.B., Einaudi, M.T., and Kunze, K., 2005, Copper deposition during quartz dissolution by cooling magmatic-hydrothermal fluids: The Bingham porphyry: Earth and Planetary Science Letters, v. 235, p. 229–243.

Leeman, W.P., MacRae, C.M., Wilson, N.C., Torpy, A., Lee, C.-T.A., Student, J.J., Thomas, J.B., and Vicenzi, E.P., 2012, A study of cathodoluminescence and trace element compositional zoning in natural quartz from volcanic rocks: Mapping titanium content in quartz: Microscopy and Microanalysis, v. 18, p. 1322–1341.

Lehmann, K., Berger, A., Götte, T., Ramseyer, K., and Wiedenbeck, M., 2009, Growth-related zonations in authigenic and hydrothermal quartz characterized by SIMS-, EPMA-, SEM-CL and SEM-CC imaging: Mineralogical Magazine, v. 73, p. 633–643.

Llovet, X., Pinard, P.T., Donovan, J.J., and Salvat, F., 2012, Secondary fluorescence in electron probe microanalysis of material couples: Journal of Physics D: Applied Physics, v. 45, p. 1–22.

Lund, K., Aleinikoff, J.N., and Kunk, M.J., 2005, Geochronologic evidence of multiple overlapping, fracture-controlled magmatic and hydrothermal pulses in the Butte District: Genetic implications for Ag and Cu veins and porphyry Mo: Geological Society of America Abstracts with Programs, v. 37, p. 314.

Lund, K., Aleinikoff, J.N., Kunk, M.J., Unruh, D.M., Zeihen, G.D., Hodges, W.C., Du Bray, E.A., and O'Neill, J.M., 2002, SHRIMP U-Pb and $^{40}Ar/^{39}Ar$ age constraints of relating plutonism and mineralization in the Boulder Batholith region, Montana: ECONOMIC GEOLOGY, v. 97, p. 241–267.

Marshall, D.J., 1988, Cathodoluminescence of geological materials: Boston, Massachusetts, Unwin Hyman Ltd, 146 p.

Matthews, N.E., Huber, C., Pyle, D.M., and Smith, V.C., 2012, Timescales of magma recharge and reactivation of large silicic systems from Ti diffusion in quartz: Journal of Petrology, v. 53, p. 1385–1416.

Mercer, C.N., and Reed, M.H., 2013, Porphyry Cu-Mo stockwork formation by dynamic, transient hydrothermal pulses: Mineralogic insights from the deposit at Butte, Montana: ECONOMIC GEOLOGY, v. 108, p. 1347–1377.

Meyer, C., 1965, An early potassic type of wall-rock alteration at Butte, Montana: American Mineralogist, v. 50, p. 1717–1723.

Meyer, C., Shea, E.P., and Goddard, C.C., Jr., et al., 1968, Ore deposits at Butte, Montana, in Ridge, J.D., ed., Ore Deposits of the United States, 1933–1967 (Graton-Sales, Volume 2): American Institute of Mining and Metallurgical Engineers, p. 1373–1415.

Morgan, D.J., Blake, S., Rogers, N.W., DeVivo, B., Rolandi, G., Macdonald, R., and Hawkesworth, C.J., 2004, Time scales of crystal residence and magma chamber volume from modelling of diffusion profiles in phenocrysts: Vesuvius 1944: Earth and Planetary Science Letters, v. 222, p. 933–946.

Müller, A., René, M., Behr, H.J., and Kronz, A., 2003a, Trace elements and cathodoluminescence of igneous quartz in topaz granites from the Hub Stock (Slavkovský Les Mts., Czech Republic): Mineralogy and Petrology, v. 79, p. 167–191.

Müller, A., Wiedenbeck, M., van den Kerkhof, A.M., Kronz, A., and Simon, K., 2003b, Trace elements in quartz: A combined electron microprobe, secondary ion mass spectrometry, laser-ablation ICP-MS, and cathodoluminescence study: European Journal of Mineralogy, v. 15, p. 747–763.

Müller, A., Herrington, R., Armstrong, R., Seltmann, R., Kirwin, D.J., Stenina, N.G., and Kronz, A., 2010, Trace elements and cathodoluminescence of quartz in stockwork veins of Mongolian porphyry-style deposits. Miner Deposita, v. 45, p. 707–727.

Penniston-Doreland, S.C., 2001, Illumination of vein quartz textures in a porphyry copper ore deposit using scanned cathodoluminescence: Grasberg Igneous Complex, Irian Jaya, Indonesia: American Mineralogist, v. 86, p. 652–666.

Redmond, P.B., Einaudi, M.T., Inan, E.E., Landtwing, M.R., and Heinrich, C.A., 2004, Copper deposition by fluid cooling in intrusion-centered systems: New insights from the Bingham porphyry ore deposit, Utah: Geology, v. 32, p. 217–220.

Reed, M.H., and Palandri, J., 2010, Ascent and cooling of magmatic fluids: Precipitation of vein and alteration minerals [abs.], in Birkle, P, and Torres-Alvarado, I.S., eds, Proceedings of the 13th International Conference on Water-Rock Interaction: Guanajuato, Mexico, August 16–20, 2010, London, Taylor and Francis Group, p. 37–40.

Reed, M.H., Rusk, B.G., and Palandri, J., 2013, The Butte magmatic-hydrothermal system: One fluid yields all alteration and veins: Economic Geology, v. 108, p. 1379–1396.

Richards, J.P., 2003, Tectonomagmatic precursors for porphyry Cu-(Mo-Au) deposit formation: Economic Geology, v. 98, p. 1515–1533.

Roberts, S.A., 1975, Early hydrothermal alteration and mineralization in the Butte district, Montana: Unpublished Ph.D. dissertation, Harvard University, 157 p.

Rubin, A.M., 1995, Getting granite dikes out of the source region: Journal of Geophysical Research, v. 100, p. 5911–5929.

Rusk, B.G., 2012, Cathodoluminescent textures and trace elements in hydrothermal quartz, in Quartz: Deposits, Mineralogy and Analytics. Springer, p. 307–329.

Rusk, B.G., and Reed, M.H., 2002, Scanning electron microscope-cathodoluminescence analysis of quartz reveals complex growth histories in veins from the Butte porphyry copper deposit, Montana: Geology, v. 30, p. 727–730.

Rusk, B.G., Lowers, H.A., and Reed, M.H., 2008a, Trace elements in hydrothermal quartz: Relationships to cathodoluminescent textures and insights into vein formation: Geology, v. 36, p. 547–550.

Rusk, B.G., Reed, M.H., and Dilles, J.H., 2008b, Fluid inclusion evidence for magmatic-hydrothermal fluid evolution in the porphyry copper-molybdenum deposit at Butte, Montana: Economic Geology, v. 103, p. 307–334.

Rusk, B.G., Reed, M.H., Dilles, J.H., and Kent, A.J.R., 2006, Intensity of quartz cathodoluminescence and trace-element content in quartz from the porphyry copper deposit at Butte, Montana: American Mineralogist, v. 91, p. 1300–1312.

Rusk, B.G., Koenig, A., and Lowers, H.A., 2011, Visualizing trace element distribution in quartz using cathodoluminescence, electron microprobe, and laser ablation-inductively coupled plasma-mass spectrometry. American Mineralogist, v. 96, p. 703–708.

Rutherford, M.J., and Gardner, J.E., 2000, Rates of magma ascent, in Sigurdsson, H., ed., Encyclopedia of Volcanoes, Academic Press, p. 207–217.

Seedorff, E., Dilles, J.H., Proffett, J.M., Einaudi, M.T., Surcher, L., Stavast, W.J.A., Johnson, D.A., and Barton, M.D., 2005, Porphyry deposits: Characteristics and origin of hypogene features: Economic Geology 100th Anniversary Volume, p. 251–298.

Sillitoe, R.H., 2010, Porphyry copper systems: Economic Geology, v. 105, p. 3–41.

Sinclair, W.D., 2007, Porphyry deposits: Mineral deposits of Canada: A synthesis of major deposit types, district metallogeny, the evolution of geological provinces, and exploration methods: Geological Association of Canada, Mineral Deposits Division, Special Publication 5, p. 223–243.

Snee, L., Miggins, D., Geissman, J., Reed, M., Dilles, J., and Zhang, L., 1999, Thermal history of the Butte porphyry system, Montana: Geological Society of America Abstract with Programs, v. 31, p. 380.

Spear, F.S., Ashley, K.T., Webb, L.E., and Thomas, J.B., 2012, Ti diffusion in quartz inclusions: Implications for metamorphic time scales: Contributions to Mineralogy and Petrology, v. 164, p. 977–986.

Titley, S.R., and Beane, R.E., 1981, Porphyry Copper deposits: Economic Geology 75th Anniversary Volume, p. 214–269.

Tosdal, R.M., and Richards, J.P., 2001, Magmatic and structural controls on the development of porphyry Cu ± Mo ± Au deposits: Reviews in Economic Geology, v. 14, p. 157–181.

Turner, S., and Costa, F., 2007, Measuring timescales of magmatic evolution: Elements, v. 3, p. 267–272.

Wark, D.A., and Watson, E.B., 2006, TitaniQ: A titanium-in-quartz geothermometer: Contributions to Mineralogy and Petrology, v. 152, p. 743–754.

Wark, D.A., Hildreth, W., Spear, F.S., Cherniak, D.J., and Watson, E.B., 2007, Pre-eruption recharge of the Bishop magma system: Geology v. 35, p. 235–238.

Watt, G.R., Wright, P., Galloway, S., and McLean, C., 1997, Cathodoluminescence and trace element zoning in quartz phenocrysts and xenocrysts: Geochimica et Cosmochimica Acta, v. 61, p. 4337–4348.

Wilcock, J., Goff, F., Minarik, W.G., and Stix, J., 2013, Magmatic recharge during the formation and resurgence of the Valles Caldera, New Mexico, USA: Evidence from quartz compositional zoning and geothermometry: Journal of Petrology, v. 54, p. 635–664.